J Solid State Electrochem (2008) 12:497–509
DOI 10.1007/s10008-007-0436-8

ORIGINAL PAPER

Influence of structural defects on the electrocatalytic activity of platinum

O. V. Cherstiouk · A. N. Gavrilov · L. M. Plyasova · I. Yu. Molina · G. A. Tsirlina · E. R. Savinova

Received: 19 September 2006 / Revised: 20 August 2007 / Accepted: 20 August 2007 / Published online: 11 October 2007

Abstract Structural defects play major role in catalysis and electrocatalysis. Nanocrystalline (or nanostructured) materials composed of nanometer-sized crystallites joined via grain boundaries have been recognized for their specific structure and properties, differentiating them from single crystals, coarsely grained materials or nanometer-sized supported single-grained particles (Gleiter, Nanostruct Mater 1:1–19, 1992). In this paper, we use Pt electrodes, prepared by electrodeposition on glassy carbon and gold supports, as model nanocrystalline materials to explore the influence of grain boundaries and other structural defects on electrocatalysis of CO and methanol oxidation. We build on the recently established correlations between the nanostructure (lattice parameter, grain size, and microstrains) of electrodeposited Pt and the deposition potential (Plyasova et al., Electrochim. Acta 51:4447–4488, 2006) and use the latter to obtain materials with variable density of grain boundary regions. The activity of electrodeposited Pt in the oxidation of methanol and adsorbed CO exceeds greatly that for Pt(111), polycrystalline Pt, or single-grained Pt particles. It is proposed that active sites in nanostructured Pt are located at the emergence of grain boundaries at the surface. For methanol electrooxidation, the electrodes with optimal nanostructure exhibit relatively high rates of the "direct" oxidation pathway and of the oxidation of strongly adsorbed poisoning intermediate (CO_{ads}), but not-too-high methanol dehydrogenation rate constant. These electrodes exhibit an initial current increase during potentiostatic methanol oxidation explained by the CO_{ads} oxidation rate constant exceeding the methanol decomposition rate constant.

Keywords Nanostructured materials · Structural defects · Grain boundary · Electrocatalysis · Platinum · CO oxidation · Methanol oxidation

Dedicated to the 65th birthday of Teresa Iwasita, who has made a major contribution to the fields of electrocatalysis and electrochemistry.

O. V. Cherstiouk · L. M. Plyasova · I. Y. Molina · E. R. Savinova
Boreskov Institute of Catalysis,
Siberian Division of the Russian Academy of Sciences,
Prospekt Ak. Lavrentieva 5,
Novosibirsk 630090, Russia

A. N. Gavrilov · G. A. Tsirlina
Department of Electrochemistry, Moscow State University,
Leninskie Gory, 1 - str.3,
Moscow GSP-2 119992, Russia

E. R. Savinova (✉)
l'Ecole Européenne Chimie Polymères Matériaux,
Université Louis Pasteur,
UMR 7515, 25, rue Becquerel,
F 67087 Strasbourg Cedex 2, France
e-mail: Elena.Savinova@ecpm.u-strasbg.fr

Introduction

Understanding relations between the structure of materials and their adsorptive and catalytic properties is the focal point of electrocatalysis and heterogeneous catalysis and is of both fundamental and practical importance. Structural effects may be concerned with the influence of (1) surface crystallography, (2) size confinement, and (3) structural defects [1]. These factors affect both geometric and electronic properties of materials.

Low-index single crystals appear to be the best model surfaces for the investigation of the influence of *surface crystallography* on catalysis and adsorption. Numerous

studies confirmed structure sensitivity of various adsorption processes, heterogeneous catalytic and electrocatalytic reactions (for recent books and reviews on structural effects in electrocatalysis see, e.g., [2–5]). It has been demonstrated that catalytic activity of metal surfaces in structure-sensitive processes may be exclusively determined by the presence of defects such as low coordinated sites [6]. Stepped single crystals have served as models for unveiling the dependence of the electrocatalytic activities on the step density and have been used to study, e.g., oxygen reduction [7–9], CO [10–12], and methanol oxidation [13]. Recently, nanofaceted surfaces have been introduced into electrocatalysis with the aim to better understand an interplay of the reaction kinetics at vicinal facets [14, 15].

Catalysts utilized for practical applications are often composed of nanometer-sized (metal) particles on inert (e.g., carbon) supports. The influence of the particle size and surface crystallography on the electrocatalytic activity of supported metal nanoparticles has been widely discussed in the literature (see Wieckowski et al. [5] and references therein). The so called "negative-particle-size effects", with specific catalytic activity decaying with the decrease of the particle size, have been documented for a number of practically relevant electrochemical processes, e.g., oxygen reduction reaction [16, 17], methanol [18–20], and carbon monoxide oxidation [21–25]. Some authors, however, dispute particle size effects in the above reactions [26, 27].

Much less is known about the influence of *defects in the bulk crystalline structure* of materials on their sorptive and catalytic properties. This influence may be manifold. In particular, bulk defects may affect sorption of foreign atoms in the material bulk [28]. Extended bulk defects, emerging at the surface, may create surface defects, and thus, influence surface processes. In the 1960s–1970s of the 20th century, a number of studies was published by the Russian school of electrochemistry devoted to the influence of various thermal, mechanical, chemical, and electrochemical treatments on the adsorptive and electrocatalytic properties of polycrystalline metals: Pt [29–31], Ni [32], Fe [33]. These led the authors to the conclusion that dislocations, emerging at the surface, create surface defects increasing hydrogen adsorption energy.

Of particular interest are nanocrystalline (addressed also as "nanostructured") materials composed of nanometer-sized crystallites joined via grain boundaries. High volume density of disordered grain boundary regions entail unique physical properties differentiating these materials from single crystals, coarsely grained materials or nanometer-sized supported single-grained particles (see, e.g., [34–36]). Nanocrystalline materials of this sort are very well-known to material scientists, but have attracted undeservedly little attention of the catalysis community. Meanwhile, positive role of grain boundaries in heterogeneous catalysis was outlined by Tsybulya et al. [37]. A correlation between the reaction rate of ethylene epoxidation and parameters responsible for the relationship among the regular and defect regions in the bulk structure of silver particles has been established.

In fact, nanocrystalline materials have been widely used in electrochemistry in the form of multilayer metal deposits, which are composed of nanometer-sized grains and contain high volume concentrations of grain boundaries and dislocations [38]. Investigations devoted to the preparation of electrodeposited metals and alloys, analyses of their structure, and their application in electrocatalysis are abundant and cannot be comprehensively reviewed within this publication. We would like to point out that Teresa Iwasita has contributed significantly to the investigation of electrocatalytic properties of electrodeposited metals [39–44].

It should be noted, however, that only a few publications addressed *specific role of grain boundary regions* in electrochemical and electrocatalytic processes. In a series of publications, Tsirlina et al. [45–48] investigated hydrogen sorption in nanostructured Pd, obtained through electrodeposition. They discovered a strong dependence of the hydrogen sorption [46–48] and adsorption [45] on the Pd deposition potential and associated it with the density of defect regions in the metal lattice. In electrocatalysis, of importance are greatly enhanced specific catalytic activities of electrodeposited Pt in CO, methanol, and ethylene glycol oxidation compared to polycrystalline Pt foil or single-grained supported Pt nanoparticles documented, .e.g., in [23, 24, 49, 50]. The activity enhancements were attributed to the high grain boundary density. It was proposed that catalytically active sites in nanostructured materials are located at the emergence of grain boundaries at the surface. It is likely that unique properties of electrodeposited metals are largely due to the interplay of bulk and surface defects in their structure.

It is worth mentioning that nanocrystalline materials are highly relevant to the practical applications. For example, catalytic layers of low-temperature fuel cells contain supported catalysts, usually with high metal percentage. High density of metal particles on the surfaces of support materials occasionally results in formation of nanostructured metals, and may have far-reaching consequences for electrocatalysis as confirmed for carbon-supported monometallic Pt and bimetallic PtRu electrodes in [50, 51].

In our recent publication [52], it was demonstrated that the deposition potential can be used as a means for tuning nanostructure of electrodeposited Pt and preparing materials with defined defect density. The present work is aimed at furthering understanding of the relationships between the defect density in Pt materials, on the one hand, and their adsorptive and electrocatalytic properties, on the other

hand. Platinum electrodeposits on glassy carbon (GC) and Au are utilized as model materials reflecting complex structural features of real catalysts, which cannot be accounted for by single crystals or supported single-grained nanoparticles.

Experimental

Materials

Solutions were prepared from Milli-Q water (18 MOhm·cm), H_2SO_4 (puriss. p.a., Fluka) and methanol (99.9%, redistilled). GC plates (1-mm thick; NIIGRAFIT, Russia; heat treated at 1,300°C) were mechanically polished to a mirror finish and cleaned repeatedly with ethanol, acetone, and water in an ultrasonic bath before the electrode preparation. H_2PtCl_4 was prepared from Pt foil (99.999) using the procedure described in [53].

Electrode preparation

Working electrodes were prepared via Pt electrodeposition on either gold foil or GC plates. The samples are further designated as Pt(ed#E_d)/Au and Pt(ed#E_d)/GC, respectively, with the deposition potential E_d indicated in the brackets. Thus, Pt(ed#0.1)/GC denotes Pt electrodeposited on GC at 0.1 V vs RHE. Pt deposition was performed from H_2PtCl_6 + HCl solutions at a constant potential, which was varied in the range from 0.025 to 0.55 V RHE. Typical Pt loadings amounted to 0.5–0.7 mg cm^{-2} for Pt/Au and to 0.1–0.2 mg cm^{-2} for Pt/GC, as for the latter, the adhesion at higher loadings was not satisfactory. For further details of the sample preparation, the reader is referred to [52]. Before electrocatalytic studies, the samples were aged under potentiodynamic conditions as described in [52].

For comparison, some measurements were performed with polycrystalline foil Pt(pc) and with GC-supported single-grained Pt nanoparticles Pt(nano)/GC prepared by chemical deposition. Their preparation procedure is described in [24].

Electrochemical measurements

Electrochemical measurements were carried out in three-electrode glass cells at 20±1°C after deaeration with Ar. The counter electrode was Pt foil and the reference electrode—either a reversible hydrogen electrode (RHE) or a mercury sulfate electrode (MSE) $Hg|Hg_2SO_4|0.1$ M H_2SO_4 (aq) connected to the cell via a Luggin capillary. Electrode potentials were controlled using Autolab PGSTAT30 potentiostat, and hereinafter, are given vs RHE (E_{MSE}=0.73 V vs RHE).

For CO stripping, CO was bubbled through the electrolyte for 15 min while the electrode was kept at a constant potential of 0.1 V, and then, dissolved CO was removed by purging the solution with Ar for 35 min. Methanol (MeOH) oxidation experiments were performed for Pt/GC using cyclic voltammetry and chronoamperometry in 0.1 M H_2SO_4+0.1 M MeOH and for Pt/Au with steady-state voltammetry in 0.5 M H_2SO_4+0.1 M MeOH. Steady-state polarization curves were acquired under potentiostatic mode by varying the electrode potential in 20 mV increments starting from 0.8 down to 0.5 V, with an automatic switching to the next potential after satisfying the quasi-steady-state criterion. The latter was set at 1% current deviation per minute. Measuring one polarization curve typically required 5–15 h. Such long measurements were not feasible for Pt/GC samples, which contained smaller amounts of Pt and were thus more readily contaminated. Current densities were normalized to the true surface area of Pt-determined coulometrically from the hydrogen desorption in supporting sulfuric acid solutions.

Electrode characterization

X-ray diffraction (XRD) patterns were acquired for Pt electrodeposits without their separation from Au or GC substrate and were recorded using URD-63 diffractometer (Germany) with monochromatic Cu $K_\alpha-$ radiation in the reflection mode. The X-ray diffraction patterns were collected in 2θ interval from 30 to 100° in 0.02° steps, the accumulation time was set in the range from 10 to 100 s depending on the reflection intensities. The average effective size of coherently scattering domains D and the crystal lattice microstrains $\Delta d/d$ were determined using Voight analysis [54]. For more details see [52].

Pt(nano)/GC samples were characterized with transmission electron microscopy (TEM) with the help of JEM-2010 instrument with a lattice resolution of 1.4 Å and an accelerating voltage of 200 kV. Samples for electron microscopy were prepared by scraping the active layer off GC support and fixing the resulting powder on «holey» carbon films supported on copper grids. The average d_N, and the surface average d_S particle size were calculated from size distributions as follows: $d_N = \sum_i d_i \Big/ \sum_i N_i; d_S = \sum_i d_i^3 \Big/ \sum_i d_i^2.$

Results and discussion

Structural characterization

In depth structural analyses of Pt electrodeposits on Au and GC supports were performed using XRD, TEM, scanning electron microscopy (SEM), and scanning tunneling

microscopy and described in [52, 55, 56]. In Plyasova et al. [52], we explored the influence of the electrodeposition potential on the structure. For convenience, we furnish the reader with a synopsis of this study, while the details can be found in the original publications [52, 55, 56].

Structural characterization complemented with the analysis of deposition transients brought us to the conclusion that specific structural features of multilayered Pt deposits result from the interplay between the primary (on the support surface) and the secondary (on the surface of electrodeposited Pt nanoparticles) nucleation. The resultant nanocrystalline materials, composed of randomly oriented nanometer-size domains (grains), are formed in the sequence of primary and secondary nucleation events, growth of metal nuclei in close proximity to each other, and their coalescence. Characteristic features of these materials, compared to polycrystalline Pt, are: (1) decreased lattice parameter a, (2) microstrains $\Delta d/d$, and (3) high concentration of dislocations and grain boundaries, all of them being determined by the deposition potential. As the deposition potential is shifted towards the positive, the lattice parameter is reduced, while microstrains and the concentration of dislocations and grain boundaries rise (Table 1).

Dislocation densities N in the boundary regions of nanocrystalline materials may be estimated from X-ray diffraction data as follows (see [57, 58] for details):

$$N = 3n/D^2 \tag{1}$$

Equation 1 is based on the assumption of fully coalesced cubic crystallites. Here, n is the number of dislocations per side of a cube. As the value of n is unknown, the lower limit of N was estimated with n set equal to 1. The resultant N varies markedly with the deposition potential (Table 1). Due to the nanometer size of Pt grains, N exceeds the value characteristic of Pt(pc) by more than an order of magnitude for the most defective samples.

Other specific structural features of Pt electrodeposits are microstrains $\Delta d/d$ (Table 1), which, depending on the deposition potential, change from ~0.3 to ~0.7%. These are about an order of magnitude smaller than the values typical for strained materials obtained under severe plastic deformations [57, 58]. Plastic deformations of materials are known to result in the emergence of random dislocations in the bodies of crystalline grains, which density ρ_{hkl} may be estimated as follows [57, 58]:

$$\rho_{hkl} = \frac{2\sqrt{3}(\Delta d/d)_{hkl}}{bD_{hkl}} \tag{2}$$

Here b is Burgers vector.

The values of ρ_{111} calculated using Eq. 2 are typical for electrodeposited metals and are listed in Table 1. Note that for single crystals, $\rho_{hkl} \sim 10^2$–10^3 cm^{-2}. One may also see that the value of ρ is significantly smaller than that of N, suggesting that *dislocations, localized in the grain boundary regions, are the most abundant defects in multilayered Pt electrodeposits*, dominating their specific structural properties.

Note that variation of nanostructure with the deposition potential affects also the specific surface areas of Pt deposits which range from 7 to 15 m^2 g^{-1} for Pt/Au and from 14 to 50 m^2 g^{-1} for Pt/GC. The highest specific surface areas were achieved at E_d=100 mV both for Pt(ed)/GC and for Pt(ed)/Au, suggesting that the degree of grain coalescence under these conditions is the lowest. This is in agreement with the lower values of microstrains and close to Pt(pc) lattice parameter.

Table 1 Grain size D, microstrains $\Delta d/d$, lattice parameter a, volume density of dislocations in the grain bodies ρ, and in the grain boundary regions N calculated for Pt(pc), for Pt(ed)/GC and for Pt(ed)/Au from X-ray diffractograms in <111> direction (See text for details)

Sample	E_d (V vs RHE)	D_{111} (nm)	$(\Delta d/d)_{111}$ 100%	a (Å)	ρ_{111} (10^{11} cm^{-2})	N_{111} (10^{11} cm^{-2})
Pt(ed)/GC	0.025	19	0.33	3.918 (5)	2.1	8.0
	0.100	18	0.27	3.91 (9)	1.9	9.2
	0.200	14	0.44	3.91 (7)	4.0	15.5
	0.300	14	0.49	3.91 (2)	4.2	14.3
	0.400	16	0.56	3.91 (4)	4.4	11.7
	0.550	14	0.69	3.91 (4)	6.2	14.9
Pt(ed)/Au	0.025	23	0.32	3.917 (8)	1.8	5.7
	0.050	28	0.29	3.918 (2)	1.3	3.8
	0.100	20	0.40	3.916 (8)	2.5	7.5
	0.200	24	0.59	3.91 (9)	3.1	5.2
	0.300	14	0.49	3.913 (9)	4.4	15.3
	0.400	18	0.60	3.915 (4)	4.6	9.3
	0.500	19	0.66	3.91 (6)	4.4	8.3
Pt(pc)[a]		50		3.9231		1.2

[a] Due to the low intensity of <111> reflection for textured Pt(pc), D<111> was recalculated from D<200>.

Interfacial properties

Typical cyclic voltammograms (CVs) of Pt electrodeposited on GC in supporting H_2SO_4 electrolyte are shown in Fig. 1. For clarity, the figure is furnished with labels, which mark hydrogen and oxygen adsorption/desorption peaks. A shift of the deposition potential towards the positive results in a decrease in the amplitude of hydrogen adsorption/desorption peaks at ~0.28 V ("strongly adsorbed" hydrogen H_{UPD2}) and an increase in the amplitude of peaks at ~0.12 V ("weakly adsorbed" hydrogen H_{UPD1}). Comparison of the hydrogen underpotential deposition (UPD) region for electrodeposited Pt with those for single crystalline electrodes [59, 60] allows to tentatively attribute these changes to a growth of the contribution of (110)-type and a decrease of the contribution of (100)-type sites to the surface. This is in agreement with the increase of the density of the grain boundary regions. The ratio of H_{UPD1} and H_{UPD2} amplitudes calculated from the positive sweeps of CVs is shown in Fig. 2a for Pt(ed)/GC and Pt(ed)/Au and demonstrates similar trends regardless of the nature of support, although the magnitude of the changes is larger for Pt(ed)/GC. For more information and discussion of the support effect, the reader is referred to Plyasova et al.[52].

The deposition potential affects also the position of the peak, corresponding to the reduction of Pt surface oxides ("oxygen reduction" peak E_{Od}) on the negative sweeps of CVs. The higher the deposition potential, the lower E_{Od} (Fig. 2b), suggesting that oxygen is stronger and more irreversibly bound to the surface of Pt deposited at more positive deposition potentials. This effect is observed both for Pt(ed)/GC and for Pt(ed)/Au electrodes, but is much stronger in the former case.

The data obtained indicate that a positive shift of the deposition potential, which is associated with the changes in the nanostructure of Pt deposits, leads to a systematic alteration in the state of hydrogen and oxygen adsorbates on the metal surface. These may be tentatively ascribed to an increase of the contribution of defect sites formed at the emergence of domain boundaries at the surface of electrodeposited Pt.

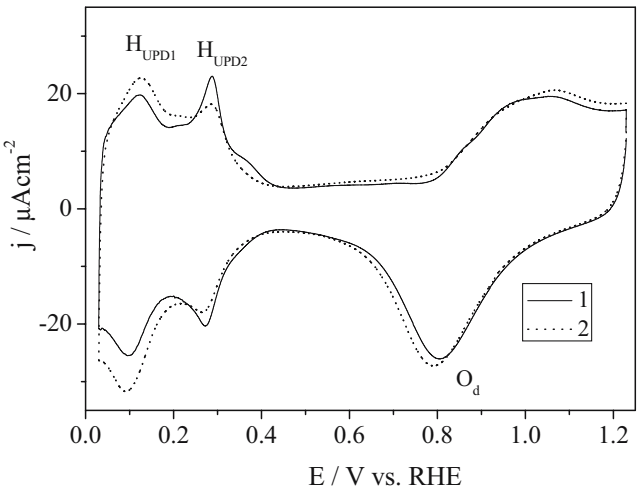

Fig. 1 Cyclic voltamogramms of Pt deposits on GC in 0.1 M H_2SO_4 prepared at *1* 0.025, *2* 0.4 V vs RHE. Sweep rate 0.02 V s^{-1}

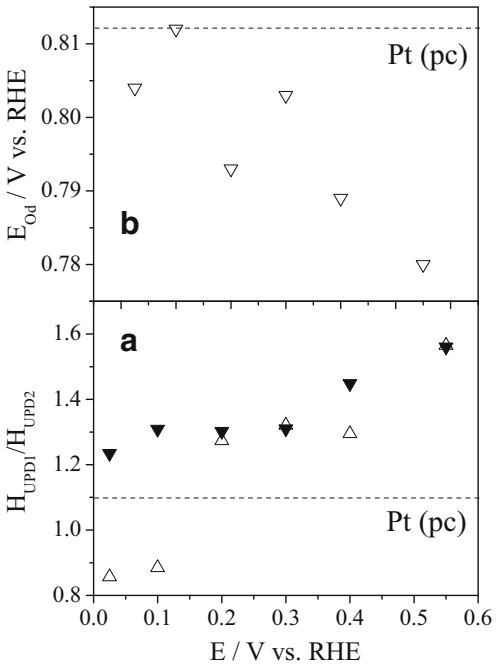

Fig. 2 Influence of the deposition potential E_d on the **a** ratio of H_{UPD1} and H_{UPD2} peak amplitudes calculated from the positive sweeps of CVs taken in 0.1 M H_2SO_4 for Pt/GC (*open symbols*) and in 0.5 M H_2SO_4 for Pt/Au (*filled symbols*) and **b** surface oxide reduction peak E_{Od} for Pt/GC. Sweep rate 0.02 V s^{-1}. The notations are explained in Fig. 1. The corresponding values for Pt(pc) are shown with the *dashed lines*

Electrocatalytic activity of Pt/GC

CO oxidation

Figure 3 shows CO stripping voltammograms for Pt(ed)/GC prepared at different deposition potentials (curves 1,2). The position of CO oxidation peak shows little dependence on the deposition potential, but for all electrodeposited samples, the peak is negatively displaced compared to polycrystalline Pt (curve 3) and Pt(nano)/GC (curve 4). Note that the saturation CO coverages for the samples explored are not the same, hence, the differences in the stripping peak areas.

More facile CO oxidation kinetics on Pt(ed)/GC compared to Pt(nano)/GC and Pt(pc) is confirmed also by chronoamperometry. Figure 4 shows CO monolayer oxidation transients registered at constant electrode potential of 0.73 V for Pt electrodes with different nanostructures.

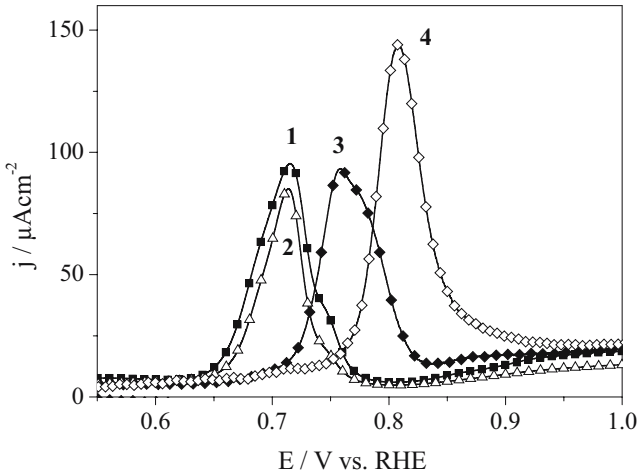

Fig. 3 CO stripping voltammograms in 0.1 M H_2SO_4 for Pt(ed)/GC electrodeposited at 0.100 (*1*) and at 0.300 (*2*) V vs RHE. For comparison, data for polycrystalline Pt (*3*) and for Pt(nano)/GC (d_N= 2.8 nm; d_S=3.4 nm) chemically deposited on GC (*4*) are shown. The latter are replotted from Maillard et al. [96] with permission from Elsevier. Sweep rate 0.02 V s^{-1}, CO adsorption potential 0.1 V RHE

These exhibit peaked shape which is in agreement with the Langmuir–Hinshelwood mechanism of CO oxidation [61]:

$$H_2O \leftrightarrow OH_{ads} + H^+ + e^- \quad (3)$$

$$CO_{ads} + OH_{ads} \xrightarrow{k_{ox}} CO_2 + H^+ + e^- \quad (4)$$

Investigation of CO oxidation at stepped Pt single crystal surfaces both in UHV [62–65] and in electrochemical environment [11, 12] has decisively proven that formation of chemisorbed oxygen-containing species (reaction 3) occurs preferentially at low coordinated sites—steps and defects, CO_{ads} from terraces reacting with O_{ads}/OH_{ads} at the steps. Different kinetic models have been set up and applied for fitting experimental transients on single crystal and nanostructured surfaces. Their detailed discussion is beyond the scope of this paper and is presented, e.g., in Andreaus et al. [66]. To account for heterogeneous surfaces of nanoparticulate and nanostructured electrodes, a mathematical model employing the active site concept was proposed in Andreaus et al. [66]. This model, assuming that OH_{ad} formation is restricted to the active sites, reproduces very well experimental transients for single- and multiple-grained GC-supported Pt nanoparticles. In depth analyses of various kinetic parameters affecting the peak shape in chronoamperograms were provided [66]. The time of the maximum (t_{max}) is determined by the fraction of the active sites on the surface, the rate constants for OH_{ads} formation at the active sites, and CO_{ads} + OH_{ads} recombination.

Figure 5 shows log(t_{max}) vs E_{ox} for Pt electrodeposited on GC at various deposition potentials, Pt(nano)/GC, and for comparison, for Pt(111) and Pt(110) from Lebedeva et al. [11]. The decrease of $t_{max}(111) > t_{max}(110) \geq t_{max}(ed)$ reflects acceleration of the CO oxidation kinetics. t_{max} exhibits minor dependence on the deposition potential; at low oxidation potentials electrodeposited Pt is even more active than Pt(110).

The grain size of electrodeposited Pt varied from ca. 14 nm at E_d=0.550 V to ca. 19 nm at E_d=0.025 V vs ca.

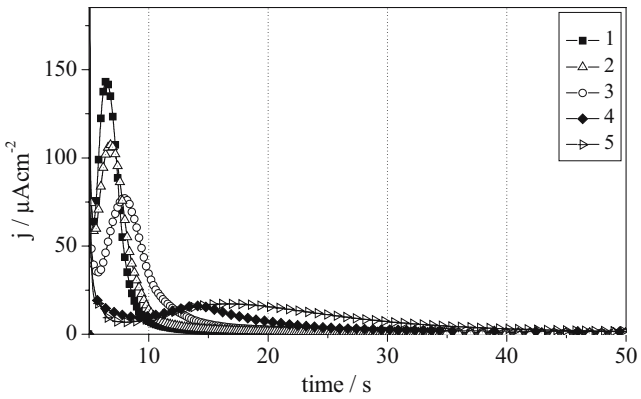

Fig. 4 Current transients for CO monolayer oxidation in 0.1 M H_2SO_4 after a potential step from 0.1 to 0.73 V vs RHE for Pt(ed)/GC prepared at different deposition potentials: 0.025 (*1*), 0.100 (*2*), 0.300 (*3*) V vs RHE. For comparison data for polycrystalline Pt (*4*) and for Pt nanoparticles (d_N=3.3 nm; d_S=5.3 nm) chemically deposited on GC (*5*) are shown. The latter are replotted from Maillard et al. [96] with permission from Elsevier. CO adsorption potential 0.1 V vs. RHE

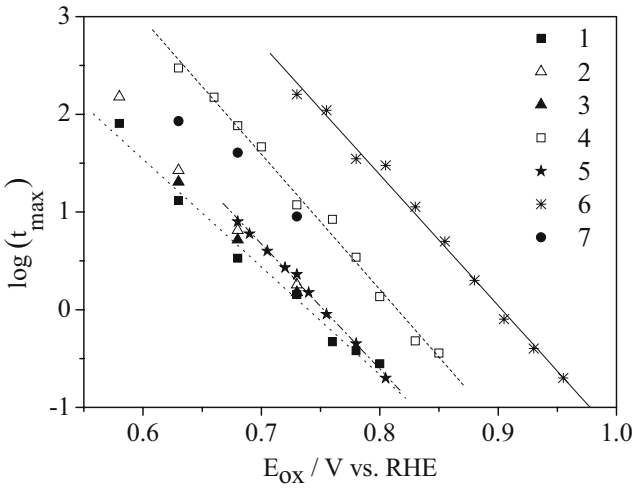

Fig. 5 Plot of the logarithm of time (in seconds) corresponding to the current maximum (t_{max}) in CO oxidation transients against the final potential for Pt(ed)/GC prepared at different deposition potentials: *1* 0.100, *2* 0.300, *3* 0.550 V vs RHE. *4* shows data for Pt nanoparticles (d_N=3.3 nm; d_S=5.3 nm) chemically deposited on GC and replotted from Maillard et al. [96] with permission from Elsevier. *5* and *6* show data for Pt(110) and Pt(111), respectively, measured in 0.5 M H_2SO_4 and replotted from Lebedeva et al. [11] with permission from ACS. Data for polycrystalline Pt are shown in *7*. CO adsorption potential 0.1 V vs RHE. The *lines* are linear fits of the experimental data

50 nm for Pt(pc). These grain dimensions are well beyond the particle size range where size effects may be expected. Indeed, it has recently been demonstrated [23–25, 67] that particle size effects in CO monolayer oxidation occur in the range from ~1 to ~4 nm, the reaction overpotential decreasing with the size. Given the grain dimensions of electrodeposited Pt and its higher [compared to Pt(pc) or Pt (nano)/GC] electrocatalytic activity in CO_{ads} oxidation, the observed structural effects can hardly be attributed to the influence of the grain size. Accelerated CO oxidation on nanostructured Pt has been mentioned in a number of publications [68–70]. Cherstiouk et al. [23] and later on Maillard et al. [50] associated this activity enhancement to the catalytic role of grain boundaries interconnecting Pt crystallites. In what follows, this hypothesis will be further verified.

Methanol oxidation

Cyclic voltammetry CVs in 0.1 M MeOH+0.1 M H_2SO_4 are shown in Fig. 6. Typical of nonsteady-state CVs for MeOH oxidation on Pt electrodes, these exhibit strong hysteresis between the positive and the negative going scans. All electrodeposited electrodes show significantly enhanced peak current densities compared to Pt(pc) and Pt (nano)/GC.

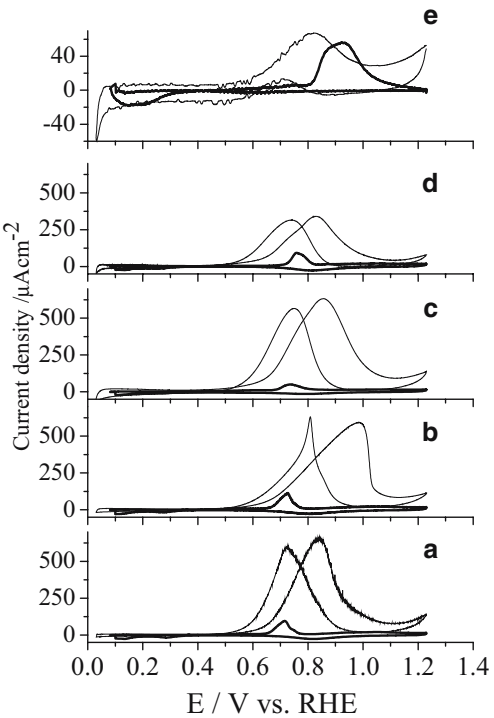

Fig. 6 CVs in 0.1 M MeOH+0.1 M H_2SO_4 (*thin solid lines*) measured at 0.02 V s^{-1} for Pt(ed)/GC prepared at different deposition potentials: **a** 0.100, **b** 0.200, **c** 0.550 V vs RHE. **d** shows data for polycrystalline Pt foil and **e** for Pt(nano)/GC (d_N=1.3 nm; d_S= 1.7 nm). *Thick solid lines* show CO stripping voltammograms for respective samples measured at the same sweep rate. In **e**, CO stripping was performed at 0.1 V s^{-1}, but the resulting current was normalized by multiplying by 0.2 and background-subtracted

Comparison of CVs for MeOH oxidation with the corresponding CO stripping voltammograms shown in Fig. 6 with thick solid lines indicates that (1) MeOH oxidation starts in the potential interval below the onset of the main CO stripping peak; (2) MeOH oxidation current densities (j_{MeOH}) for Pt(ed)/GC exceed greatly those corresponding to CO ML oxidation (j_{CO}), while for Pt (nano)/GC, j_{MeOH} and j_{CO} are comparable. To analyze the experimental data, we briefly review the current state of the understanding of the methanol electrooxidation mechanism.

MeOH oxidation on Pt electrodes has been under careful attention of electrochemists for several decades (see, e.g., review articles [71–77]). The main features of this complex multistep reaction have already been described in the seminal paper by Petrii et al. published in 1965 [77]. The reaction occurs through a sequence of MeOH dehydrogenation/decomposition steps leading to formation of a strongly adsorbed intermediate, inhibiting the reaction. A large gap has been noticed between the initial and the steady-state oxidation rates and attributed to the reaction self-inhibition. During the last decades, most of the conclusions of this paper found additional experimental support from spectroscopic techniques, including infrared spectroscopy (IR) and differential electrochemical mass spectroscopy (DEMS).

According to the present understanding, methanol oxidation on Pt electrodes occurs via the "dual-path" mechanism [78]. The so-called "indirect" pathway occurs as described above and involves (1) MeOH dissociative adsorption and formation of strongly adsorbed CH_xO_{ads} intermediates and (2) oxidation of these adsorbates in a Langmuir–Hinshelwood type reaction via interaction with chemisorbed oxygen-containing species (usually denoted as OH_{ads}). Equation 5 describes complete dehydrogenation leading to CO_{ads}, while Eq. 4 describes the oxidation of the latter. Based on the investigations of MeOH oxidation with the electrochemical methods [79, 80], in situ IR spectroscopy [81–85] and online DEMS [81, 86–91], COH_{ads} and CO_{ads} have been identified as the main adsorbates, the latter being abundant in the potential interval of continuous MeOH oxidation. The second, the so-called "direct" pathway is postulated to occur through a "reactive intermediate" (RI), which is different from CO_{ads} and is less strongly bonded to the electrode surface. Formation of some weakly bonded intermediates which can be easily washed away from the electrode surface has been mentioned already by Petrii et al. [77]. The term "direct pathway" may sound somewhat misleading, but corresponds to the pathway which avoids formation of strongly

adsorbed poisoning intermediates. It results in a stepwise oxidation of MeOH (Eq. 6) to form formaldehyde, formic acid, and ultimately CO_2 [74, 84, 85, 92].

$$CH_3OH \xrightarrow{k_{dec}} CO_{ads} + 4H^+ + 4e^- \quad (5)$$

$$CH_3OH \xrightarrow{k_d} RI \rightarrow \text{partial oxidation products} \rightarrow CO_2 \quad (6)$$

Recently, Batista et al. [85, 93] proposed that partitioning between "direct" and "indirect" pathway occurs already at the first dehydrogenation step. C–H bond splitting and formation of hydroxymethyl CH_2OH_{ads} adsorbate further leads to CO_{ads} ("indirect" pathway) as earlier proposed by Petrii et al. [77]. Meanwhile, O–H bond splitting and formation of reactive methoxy-adsorbate CH_3O_{ads} is believed to lead to formaldehyde ("direct" pathway). Neurock, using ab initio quantum chemical methods, provided solid basis for the above hypothesis [94], and demonstrated the influence of the electrode potential and the solvent on the elementary adsorption and oxidation steps. Further support has been provided by Housmans et al. [95] in their online electrochemical mass spectrometry investigation of the methanol oxidation pathways on the basal and stepped Pt single crystalline electrodes in sulfuric and perchloric acid electrolytes. The results indicate that branching between "direct" and "indirect" pathways is critically dependent on the surface crystallography and presence of surface defects (steps). It was suggested that (110) steps catalyze the direct pathway.

Comparison of CVs for methanol and for CO monolayer oxidation suggests that for Pt(ed)/GC, the "direct" pathway is much more important than for Pt(pc) and particularly for Pt(nano)/GC, and under some experimental conditions, may become predominant. Indeed, when the electrode potential is cycled in the presence of MeOH, H_{UPD} region is strongly suppressed, suggesting that the surface of Pt is poisoned by strongly adsorbed CO_{ads}. Under these conditions, observation of MeOH oxidation currents greatly exceeding the current associated with CO_{ads} oxidation, suggests occurrence of an alternative reaction pathway on the free surface sites. It is thus likely that the "direct" pathway is accelerated by the presence of the grain boundary regions. For gaining more information on the influence of nanostructure on the MeOH oxidation kinetics, chronoamperometry was used.

Chronoamperometry MeOH oxidation transients registered for selected Pt(ed)/GC at three different electrode potentials are shown in Fig. 7. Apparently, the electrode structure exerts strong influence on the current densities and on the shapes of the transients. For Pt(ed)/GC obtained at $E_d \geq$ 0.2 V decaying transients typical for processes with self inhibition are observed (see Fig. 7a,b). For Pt(ed)/GC prepared at low deposition potentials (0.025 and 0.1 V), transients with the initial current increase are observed at selected oxidation potentials (see Fig. 7c). Rising transients have also been obtained for Pt(ed#0.1)/Au. Similar transients were observed for Pt(111) by Housmans and Koper

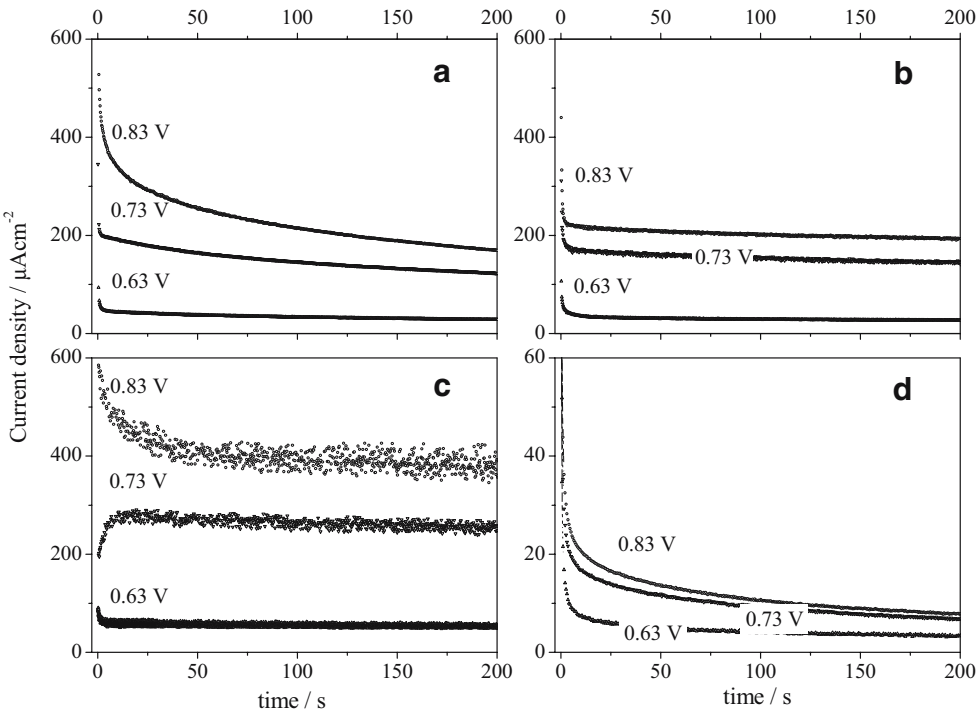

Fig. 7 Current transients in 0.1 M MeOH+0.1 M H_2SO_4 after potential steps from 0.1 V to 0.63 V, 0.73 V and 0.83 V for Pt(ed)/GC prepared at different deposition potentials: (**a**) 0.550, (**b**) 0.200, (**c**) 0.100 V vs. RHE and (**d**) for Pt(nano)/GC (d_N=1.3 nm; d_S=1.7 nm). Step potentials are indicated in the plots. Note different scale in panel (**d**)

[13] and attributed to CO oxidation being faster than the methanol dissociative adsorption. However, in contrast to low catalytic activity of Pt(111), electrodeposited Pt samples are characterized by very high specific catalytic activities.

To better understand the influence of the deposition potential (and ultimately the electrode structure) on the MeOH oxidation kinetics, we tried to fit the experimental transients with a simplified kinetic model, including (1) methanol dissociative adsorption (or decomposition) with the rate constant k_{dec} (Eq. 5), (2) oxidation of the adsorbed intermediates with the rate constant k_{ox} (Eq. 4), and (3) "direct" MeOH oxidation with the rate constant k_d (Eq. 6). For simplicity, CO_{ads} was considered as an abundant adsorption species and the "direct" oxidation pathway assumed to have no common steps with the "indirect" pathway. Chemisorbed oxygen-containing adsorbates were designated as OH_{ads}. Under the above assumptions, the overall MeOH oxidation current density can be expressed as a sum of currents (Eq. 7), corresponding to reactions 4, 5, and 6:

$$j_{total} = j_{dec} + j_{ox} + j_d \tag{7}$$

Current densities corresponding to individual reaction steps can be expressed as [13]:

$$j_{dec} = 4eN_{Pt}k_{dec}\left(1 - \sum_i \theta_i\right)^n \tag{8}$$

$$j_{ox} = 2eN_{Pt}k_{ox}^{'}\theta_{CO}\theta_{OH} \tag{9}$$

$$j_d = j_d^0 \cdot \left(1 - \sum_i \theta_i\right) \tag{10}$$

Here, N_{Pt} is the number of Pt atoms per cm^2 (1.5×10^{15}), e is the elementary charge (1.6022×10^{-19} C), j_d^0 corresponds to the current density of "direct" pathway on the Pt surface free from the adsorbates. The rate constant k_{dec} implicitly includes MeOH concentration.

To diminish the number of adjustable parameters and simplify the resulting kinetic equation the following assumptions were made: (1) $n\approx1$ (as estimated from the initial part of the current transients); (2) $\sum_i \theta_i \approx \theta_{CO}$; (3) C_{MeOH} = const; (4) $\theta_{CO}^{max} = 1$ and (5) θ_{OH} = const and equal to the fraction of active sites on the surface. The model considered is very similar to the model proposed by Housmans and Koper [13] for fitting MeOH electrooox-idation transients at stepped Pt single crystals except for (1) and (5). In the model considered in Housmans and Koper [13], n=2 and $\theta_{OH} = 1 - \theta_{CO}$. We consider the assumption $\theta_{OH} = 1 - \theta_{CO}$ to be hardly applicable to very heterogeneous surfaces of nanostructured electrodes utilized in this work.

Under the above simplifying assumptions, one obtains:

$$j_{total} = j_d^0 \cdot (1 - \theta_{CO}) + 4eN_{Pt}k_{dec}(1 - \theta_{CO}) + 2eN_{Pt}k_{ox}\theta_{CO} \tag{11}$$

$$\frac{d\theta}{dt} = k_{dec}(1 - \theta_{CO}) - k_{ox}\theta_{CO} \tag{12}$$

Figure 8 shows some selected experimental transients and their fits with the model described. Although the quality of the fits is not always satisfactory, the simplified model is able to predict a change in the shape of the transients from decaying to rising when k_{ox} exceeds k_{dec}, similar to the model considered by Housmans and Koper [13]. The limitations of the model are (1) the inability to describe the decrease of the current at t>100 s and (2) zero values of j_d which is admittedly incorrect. We have tried fitting with different models, including the one proposed by Housmans and Koper [13]. However, this did not improve substantially the quality of the fits. We suppose that kinetics

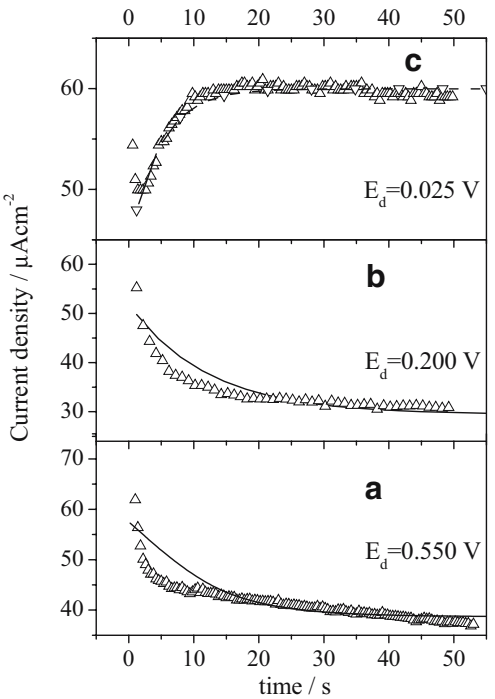

Fig. 8 Current transients in 0.1 M MeOH+0.1 M H_2SO_4 after potential steps from 0.1 to 0.63 V for Pt(ed)/GC prepared at different deposition potentials: **a** 0.550, **b** 0.200, **c** 0.025 V vs RHE. The *symbols* show the experimental data. The lines correspond to the fits. The following parameters are obtained from fitting: **a** k_{dec}=0.049, k_{ox}/k_{dec}=1.17; **b** k_{dec}=0.039, k_{ox}/k_{dec}=1.09; **c** k_{dec}=0.056, k_{ox}/k_{dec}=2.80. See text for further details

of MeOH oxidation on highly heterogeneous surfaces of electrodeposited Pt, which comprise both regular and defect crystal lattice domains, is more complicated than on single crystalline surfaces.

Steady-State polarization Figure 9 shows E vs log$j$-curves (Tafel plots) obtained for Pt(ed)/Au using steady-state voltammetry in the electrode potential interval from 0.55 to 0.65 V vs RHE. The slopes $\frac{\partial E}{\partial \log j}$ are close to linear and vary from 65 to 85 mV dec^{-1}: the higher the electrocatalytic activity, the lower the slope. The Tafel slopes and the current densities for MeOH oxidation on Pt depend on the electrode potential and on the degree of the electrode poisoning. Petrii et al. [77] documented $\frac{\partial E}{\partial \log j} \approx 60$ mVdec^{-1} for platinized platinum under steady-state MeOH oxidation and explained this by a reversible electrochemical followed by chemical *rds*, the latter attributed to the interaction of chemisorbed methanol derivatives with the oxygen-containing species.

Figure 10 compares quasistationary activities in MeOH oxidation. Similar trends have been documented for Pt(ed)/GC and Pt(ed)/Au: the activities are the highest for the samples prepared at 0.1 V, decreasing for both higher and lower deposition potentials. First of all, this suggests that the electrocatalytic activities are determined by the deposition potential rather than by the type of support. Second, this attests for reliability of the trends described, as Pt(ed)/Au and Pt(ed)/GC samples were prepared and studied in two different laboratories in Moscow and Novosibirsk, respectively. The same trend has been observed for specific surface areas which showed maxima for the electrodes prepared at 0.1 V [52]. The observed fact formally leads us to the conclusion that the highest quasi-steady-state activities of MeOH oxidation are achieved for electrodeposited samples with the lowest degree of coalescence of the crystalline domains, and hence, the lowest defect densities. This seems to be in contradiction to the catalytic role of grain boundaries declared in "Introduction". We will attempt to resolve this seeming discrepancy in "Catalytic properties as related to the defect density".

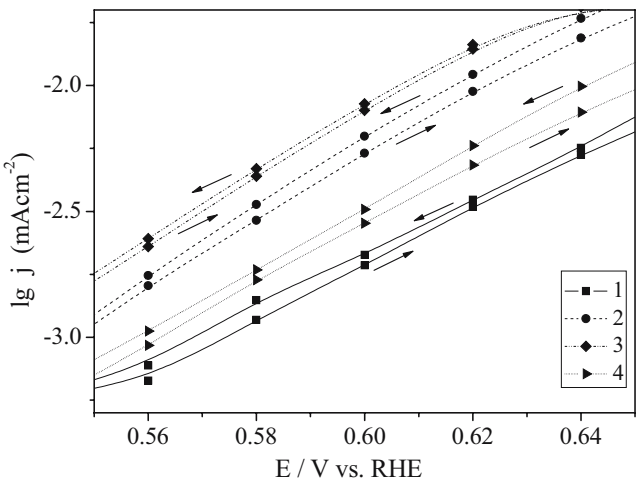

Fig. 9 Stationary polarization curves for methanol oxidation on Pt/Au measured in 0.1 M CH_3OH+0.5 M H_2SO_4 solution. E_d=0.500 (*1*), 0.400 (*2*), 0.100 (*3*), 0.025 (*4*). For each electrode, two curves are shown and indicated by *arrows*: one measured in cathodic, another one in anodic direction

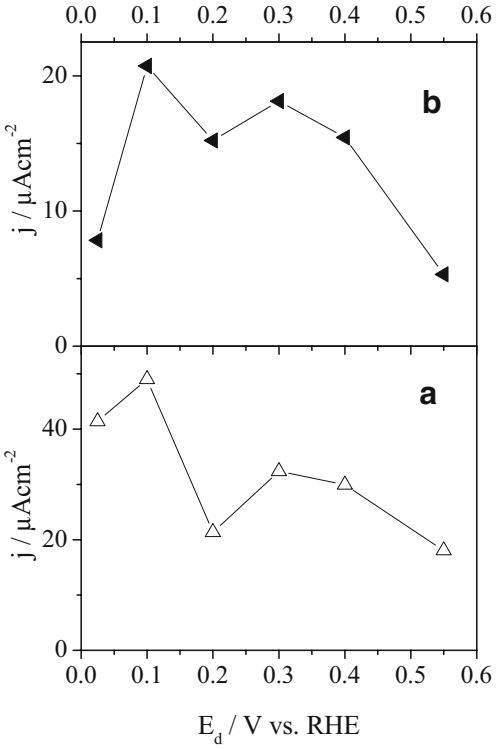

Fig. 10 Influence of the deposition potential on the quasi-steady-state current densities for MeOH oxidation for Pt(ed)/GC measured from chronoamperograms at 0.63 V and t=650 s (**a**) and for Pt(ed)/Au measured from stationary polarization curves at 0.64 V (**b**). *Lines* are guides for the eye

Catalytic properties as related to the defect density

Although some indications concerning the influence of the density of defects in the bulk crystalline structure of materials on the adsorptive and (electro)catalytic properties of materials can be found in the literature, direct correlations between these are scarce. A rare and impressive example is the already mentioned correlation between the rate of ethylene epoxidation and the ratio between the particle size measured by TEM and XRD (D_{TEM}/D_{XRD}), which is proportional to the number of grain boundaries in multi-grain particles [37].

In this article, we seek for a correlation between the density of structural defects in Pt electrode materials and their electrocatalytic properties. As discussed in "Structural characterization", dislocations in the grain boundary

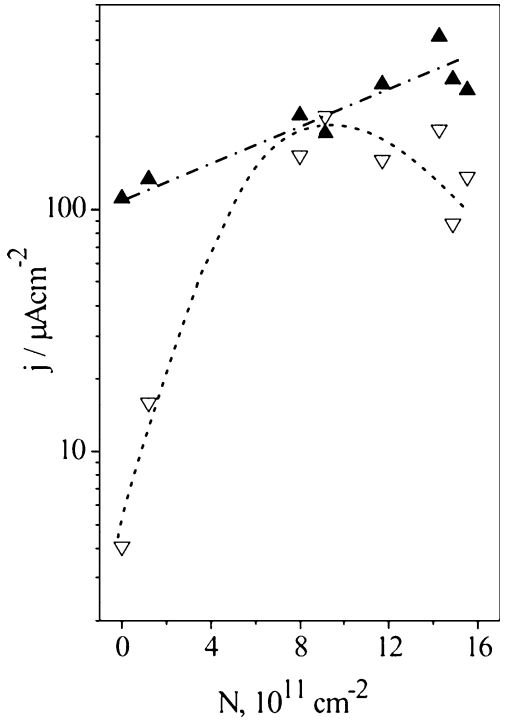

Fig. 11 MeOH oxidation current density at 0.73 V vs RHE measured in 0.1 M CH_3OH+0.1 M H_2SO_4 vs the grain boundary density N for various Pt electrodes. *Filled symbols* show current density measured after 0.2 s, *empty symbols* show current density after 650 s of the electrolysis. Lines are guides for the eye. See text for details

regions have been identified as abundant defects in electrodeposited Pt. In Fig. 11, the current densities for MeOH oxidation at 0.73 V RHE are plotted vs N[1]. Except for Pt (ed)/GC, the data for Pt(pc) and Pt(nano)/GC are included to explore the versatility of the correlation. For Pt(nano)/GC, the grain boundary concentration was assumed zero, as according to HRTEM data, each Pt particle in the sample comprised a single grain. Current densities were calculated from potentiostatic current transients. Current density at t=0.2 s, j(0.2), was taken as an apparent characteristic of the catalytic activity of an essentially unpoisoned surface, while current density after 650 s, j(650), as a characteristic of quasi-steady-state activity of the poisoned surface. It should be noted that at 0.2 s, the charging current is negligibly small.

One may see that j(0.2) increases with the growth of the defect density, being the lowest for Pt(nano)/GC, increasing somewhat for polycrystalline Pt and increasing again for electrodeposited Pt. The spread between different samples makes up to the factor of 5 (note the log scale). Meanwhile, j(650) shows a volcano type behavior. Pt(nano)/GC (N~0) exhibits the lowest j(650), as the current drops by a factor of ca. 30 during 650 s of the electrolysis. A smaller but still sizable current density drop is observed for Pt(pc) with (N=1.2 × 10^{11} cm^{-2}). Meanwhile, for Pt(ed#0.1)/GC (N= 9.2 × 10^{11} cm^{-2}), no poisoning is observed, the activity increasing with the time. Further growth of N leads, however, to the increase of the extent of the electrode poisoning, and thus, results in lower quasi-steady-state activities.

Pt(ed#0.1)/GC seems to comprise an optimal density of defects. This can be rationalized as follows. According to the present understanding, the activity of unpoisoned Pt electrodes at short reaction times is determined by the rate of MeOH dehydrogenation (Eq. 5) and the rate of "direct" MeOH oxidation (Eq. 6). The positive effect of defects on j (0.2) indicates that either of these reactions or both be catalyzed by defects. This is in agreement with the results obtained by Housmans and Koper [13] on the positive effect of steps on k_{dec} and k_d at high index Pt single crystals. An increase of k_{dec}, unless it is accompanied by a concomitant increase of k_{ox}, must result in an increase in the extent of poisoning. As demonstrated in "CO oxidation", the CO oxidation activity increases greatly from Pt (nano) to Pt(pc) and then Pt(ed). The shape of the current transients changes from decaying for Pt(nano)/GC (Fig. 7d) and Pt(pc) (not shown) to rising for Pt(ed#0.100) and Pt (ed#0.025). Obviously, the increase of k_{ox} overweighs that of k_{dec}, thus, leading to the decrease of the extent of self-poisoning, the change in the shape of the transients, and thus, to the strong increase in the quasi-steady-state activity j(650). However, further increase of the defect density does not result in the further enhancement of the CO oxidation rate, as discussed in CO oxidation. Meanwhile, k_{dec} is likely to further increase, as suggested by the growth of j(0.2) and by the change of the shape of the transients, which for samples obtained at $E_d \geq 0.2$ V again becomes decaying (Fig. 7a,b). This results in an increase of the degree of self-poisoning and the concomitant decrease of j(650).

We further speculate that the mechanism through which dislocations in the grain boundary regions influence the electrocatalytic activity of Pt operates via formation of defects on the surface of nanostructured electrodes at the emergence of grain boundaries at the surface. Metal atoms in the vicinity of grain boundaries usually have decreased number of neighbors in the first coordination shell, and thus, are expected to strongly bind adsorbates and catalyze bond-breaking reactions like water dissociation and MeOH dissociative chemisorption. For complex multistep electrochemical reactions, like MeOH oxidation accompanied with self inhibition, the concentration of defects must be sufficiently high to provide high electrocatalytic activity but not-too-high to avoid high degree of self-inhibition.

[1]It is worth mentioning that qualitatively the same trends are observed whether the current is plotted vs N or ρ.

Hence, so that the highest steady-state electrocatalytic activity is attained, the electrode surfaces must comprise an optimal ratio between defect regions and ordered crystalline domains.

It has been noticed that quasi-steady-state activity in the methanol oxidation correlates with the strength of oxygen bonding as accessed from the peak potential of surface oxide reduction: the stronger oxygen is bonded to the surface, the lower is CO and methanol oxidation activity. This applies reasonably well within the series of electrodeposited samples. However, comparison of Pt electrodes prepared by different means reveals that the position of the surface oxide reduction peak alone cannot serve as a measure of the electrode electrocatalytic activity. This finding suggests that it is not the strength of oxygen bonding which directly influences the catalytic activity, but it is rather structural parameters which affect both the oxide reduction peak and the methanol oxidation activity.

Conclusions

CO and methanol oxidation have been studied on electrodeposited Pt. The deposition potential has been found to considerably influence the catalytic activity of Pt in MeOH oxidation, and to a lesser extent, in CO monolayer oxidation. This can be explained by the dependence of Pt nanostructure on the deposition potential.

The correlation between the volume density of grain boundaries between Pt crystallites and electrocatalytic activity in methanol and CO oxidation has been suggested. The initial activity of clean Pt surface in MeOH oxidation increases with the increase in the grain boundary concentration, while the quasi-steady-state activity shows a volcano-type behavior with a maximum at $N \sim 9 \times 10^{11}$ cm^{-2}. The results obtained suggest that defect regions located at the emergence of grain boundaries at the surface play an important role in electrocatalytic processes.

Materials comprising high density of grain boundaries may be of interest for practical applications, as contrary to the surface defects, like steps and kinks on flat surfaces, defects in the bulk crystalline structure usually have much longer lifetimes, unless high temperature annealing procedures are employed.

Acknowledgements Financial support by the Russian Foundation for Basic Research (RFBR) under grants No. 01-03-33132 and No. 06-03-32737 is gratefully acknowledged. The authors would like to thank Prof. S.V. Tsybulya (BIC, Novosibirsk) for stimulating discussions concerning the influence of structural defects on the catalytic properties, Prof. O.A. Petrii (MSU, Moscow) for his remarks on methanol oxidation mechanism, and Prof. M.T.M. Koper for kindly granting permission to reproduce the data from Ref. [11].

References

1. Skundin AM (1982) In: Itogi nauki i tekhniki. Elektrokhimija (Science and Engeneering Accounts. In Russ.), vol 18. VINITI, Moscow, p 228
2. Lipkowski J, Ross PN (eds) (1998) Electrocatalysis (frontiers in electrochemistry). John Wiley & Sons, New York
3. Wieckowski A (ed) (1999) Interfacial electrochemistry: theory, experiment and applications. Marcel Dekker, New York, Basel
4. Vielstich W, Lamm A, Gasteiger HA (eds) (2003) Handbook of fuel cells. Fundamentals, Technology and Applications, vol 2: Electrocatalysis. Wiley, Chichester
5. Wieckowski A, Savinova ER, Vayenas CG (eds) (2003) Catalysis & electrocatalysis at nanoparticle surfaces. Marcel Dekker, New York
6. Zambelli T, Wintterlin J, Trost J, Ertl G (1996) Science 273:1688
7. Strbac S, Anastasijevic NA, Adzic RR (1994) Electrochimica Acta 39:983
8. Maciá MD, Campiña JM, Herrero E, Feliu JM (2004) J Electroanal Chem 564:141
9. Kuzume A, Herrero E, Feliu JM (2007) J Electroanal Chem 599:333
10. Lebedeva NP, Koper MTM, Herrero E, Feliu JM, van Santen RA (2000) J Electroanal Chem 487:37
11. Lebedeva NP, Koper MTM, Feliu JM, van Santen RA (2002) J Phys Chem B 106:12938
12. Lebedeva NP, Rodes A, Feliu JM, Koper MTM, van Santen RA (2002) J Phys Chem B 106:9863
13. Housmans THM, Koper MTM (2003) J Phys Chem B 107:8557
14. Komanicky V, Menzel A, Chang KC, You H (2005) J Phys Chem B 109:23543
15. Komanicky V, Menzel A, You H (2005) J Phys Chem B 109:23550
16. Kinoshita K (1992) Electrochemical oxygen technology. Wiley, New York
17. Gasteiger HA, Kocha SS, Sompalli B, Wagner FT (2005) Appl Catal B Environ 56:9
18. Takasu Y, Iwazaki T, Sugimoto W, Murakami Y (2000) Electrochem Commun 2:671
19. Frelink T, Visscher W, van Veen JAR (1995) J Electroanal Chem 382:65
20. Park S, Xie Y, Weaver MJ (2002) Langmuir 18:5792
21. Yahikosawa K, Tateishi N, Nishimura K, Takasu Y (1992) Chem Express 7:4
22. Friedrich KA, Marmann A, Stimming U, Unkauf W, Vogel R (1997) Fresenius J Anal Chem 358:163
23. Cherstiouk OV, Simonov PA, Chuvilin AL, Savinova ER (2001) In: Wieckowski A, Brooman EW, Rudd EJ, Fuller TF, Leddy J (eds) The global climate change: a coordinated response by electrochemistry and solid-state science and technology ECS. ECS Inc., Phoenix
24. Cherstiouk OV, Simonov PA, Savinova ER (2003) Electrochimica Acta 48:3851
25. Maillard F, Eikerling M, Cherstiouk OV, Schreier S, Savinova E, Stimming U (2004) Faraday Discuss 125:357
26. Watanabe M, Saegusa S, Stonehart P (1988) Chem Lett1487
27. Yano H, Inukai J, Uchida H, Watanabe M, Babu PK, Kobayashi T, Chung JH, Oldfield E, Wieckowski A (2006) Phys Chem Chem Phys 8:4932
28. Bucur RV (1987) Acta Met 35:1325
29. Balasheva NA, Zhmakin GG (1962) Dokladi Akademii Nauk USSR 143:358
30. Pyshnograeva II, Skundin AM, Vassilyev YB, Bagotskii VS (1969) Electrokhimija 5:1469
31. Pyshnograeva II, Vassilyev YB, Bagotskii VS (1970) Electrokhimija 6:1545

32. Kudryashev IV, Izmajlov AV, Lelikov YA (1975) Zh. Fiz. Khim. (Russian Journal of Physical Chemistry) 49:929
33. Iofa ZA, Batrakov VV, Nikiforova YA (1967) Vestnik MGU, Serija Khim 6:11
34. Gleiter H (1992) Nanostruct Mater 1:1
35. Birringer R, Gleiter H (1994) In: Haberland H (ed) Clusters of atoms and molecules. Springer Series in Chemical Physics. vol. 56. Springer, Berlin, p. 384
36. Gleiter H (2000) Acta Mater 48:1
37. Tsybulya SV, Kryukova GN, Goncharova SN, Shmakov AN, Balzhinimaev BS (1995) J Catal 154:194
38. Gamburg YD (1997) Electrodeposited metals. Yanus-K, Moscow
39. de Souza JPI, Iwasita T, Nart FC, Vielstich W (2000) J Appl Electrochem 30:43
40. de Lima RB, Paganin V, Iwasita T, Vielstich W (2003) Electrochimica Acta 49:85
41. Brisard GM, Camargo APM, Nart FC, Iwasita T (2001) Electrochem Commun 3:603
42. Camara GA, de Lima RB, Iwasita T (2004) Electrochem Commun 6:812
43. Camara GA, de Lima RB, Iwasita T (2005) J Electroanal Chem 585:128
44. de Lima RB, Massafera MP, Batista EA, Iwasita T (2007) J Electroanal Chem 603:142
45. Tsirlina GA, Baronov SB, Spiridonov FM, Rusanova MY, Safonova TY, Petrii OA (2000) Russ J Electrochem 36:1179
46. Rusanova MY, Tsirlina GA, Petrii OA, Safonova TY, Vassiliev SY (2000) Russ J Electrochem 36:457
47. Petrii OA, Safonova TY, Tsirlina GA, Rusanova MY (2000) Electrochim Acta 45:4117
48. Rusanova MY, Grden M, Czerwinski A, Tsirlina GA, Petrii OA, Safonova TY (2001) J Solid State Electrochem 5:212
49. Lebedeva NP, Kryukova GN, Tsybulya SV, Salanov AN, Savinova ER (1998) Electrochimica Acta 44:1431
50. Maillard F, Schreier S, Hanzlik M, Savinova ER, Weinkauf S, Stimming U (2005) Phys Chem Chem Phys 7:385
51. Gavrilov AN, Savinova ER, Simonov PA, Zaikovskii VI, Cherepanova SV, Tsirlina GA, Parmon VN (2007) Phys Chem Chem Phys (Advance Article). doi:10.1039/b707598g
52. Plyasova LM, Molina IY, Gavrilov AN, Cherepanova SV, Cherstiouk OV, Rudina NA, Savinova, ER, Tsirlina GA (2006) Electrochim Acta 51:4477–4488
53. Brauer G (1985) Handbook of preparative inorganic chemistry, vol. 5. Mir, Moscow (Russian translation)
54. Langford JI, Delhez R, Keijser TH, Mittemeijer EJ (1988) Aust J Phys 41:173
55. Sherstyuk OV, Pron'kin SN, Chuvilin AL, Salanov AN, Savinova ER, Tsirlina GA, Petrii OA (2000) Russ J Electrochem 36:741
56. Plyasova LM, Molina IJ, Cherepanova SV, Rudina NA, Cherstiouk OV, Savinova ER, Pron'kin SN, Tsirlina GA (2002) Russ J Electrochem 38:1116
57. Williamson GK, Smallman RE (1956) Phil Mag 1:34
58. Valiev RZ, Alexandrov IV (2000) Nanostructural materials obtained by severe plastic deformation. Logos, Moscow
59. Clavilier J (1980) J Electroanal Chem 107:211
60. Lamy C, Leger JM, Clavilier J (1982) J Electroanal Chem 135:321
61. Gilman S (1964) J Phys Chem 68:70
62. Yates JT (1995) J Vac Sci Technol A-Vacuum Surfaces Films 13:1359
63. Xu JZ, Yates JT (1993) J Chem Phys 99:725
64. Xu JZ, Henriksen P, Yates JT (1992) J Chem Phys 97:5250
65. Szabo A, Henderson MA, Yates JT (1992) J Chem Phys 96:6191
66. Andreaus B, Maillard F, Kocylo J, Savinova ER, Eikerling M (2006) J Phys Chem B 110:21028
67. Cherstiouk OV, Simonov PA, Zaikovskii VI, Savinova ER (2003) J Electroanal Chem 554:241
68. Jiang JH, Kucernak A (2002) J Electroanal Chem 533:153
69. Chen W, Sun SG, Zhou ZY, Chen SP (2003) J Phys Chem B 107:9808
70. Arenz M, Mayrhofer KJJ, Stamenkovic V, Blizanac BB, Tomoyuki T, Ross PN, Markovic NM (2005) J Am Chem Soc 127:6819
71. Markovic NM, Ross PN (2002) Surf Sci Rep 45:121
72. Wasmus S, Kuever A (1999) J Electroanal Chem 461:14
73. Lamy C, Leger JM (1991) Journal De Chimie Physique Et De Physico-Chimie Biologique 88:1649
74. Sriramulu S, Jarvi TD, Stuve EM (1999) In: Wieckowski A (ed) Interfacial electrochemistry: theory, experiment, and applications. Marcel Dekker, New York, p 793
75. Waszczuk P, Lu GQ, Wieckowski A, Lu C, Rice C, Masel RI (2002) Electrochim Acta 47:3637
76. Hamnett A (1999) In: Wieckowski A (ed) Interfacial electrochemistry: theory, experiment, and applications. Marcel Dekker, New York, p 843
77. Petrii OA, Podlovchenko BI, Frumkin AN, Lal H (1965) J Electroanal Chem 10:253
78. Herrero E, Chrzanowski W, Wieckowski A (1995) J Phys Chem 99:10423
79. Bagotzky VS, Vassiliev YB (1967) Electrochim Acta 12:1323
80. Bagotzky VS, Vassiliev YB, Khazova OA (1977) J Electroanal Chem 81:229
81. Iwasita T, Vielstich W, Santos E (1987) J Electroanal Chem 229:367
82. Castro Luna AM, Giordano MC, Arvia AJ (1989) J Electroanal Chem 259:173
83. Beden B, Lamy C, Bewick A, Kunimatsu K (1981) J Electroanal Chem 121:343
84. Iwasita T (2003) In: Vielstich W, Gasteiger HA, Lamm A (eds) Handbook of fuel cells—fundamentals, technology and applications, vol 2: electrocatalysis. Wiley, Chichester, p p 603
85. Batista EA, Malpass GRP, Motheo AJ, Iwasita T (2004) J Electroanal Chem 571:273
86. Iwasita T, Vielstich W (1986) J Electroanal Chem 201:403
87. Wilhelm S, Iwasita T, Vielstich W (1987) J Electroanal Chem 238:383
88. Jusys Z, Behm RJ (2001) J Phys Chem B 105:10874
89. Jusys Z, Kaiser J, Behm RJ (2003) Langmuir 19:6759
90. Wang H, Loffler T, Baltruschat H (2001) J Appl Electrochem 31:759
91. Wang HS, Wingender C, Baltruschat H, Lopez M, Reetz MT (2001) J Electroanal Chem 509:163
92. Breiter M (1967) Electrochim Acta 12:1213
93. Batista EA, Malpass GRP, Motheo AJ, Iwasita T (2003) Electrochem Commun 5:843
94. Cao D, Lu G-Q, Wieckowski A, Wasileski SA, Neurock M (2005) J Phys Chem B 109:11622
95. Housmans THM, Wonders AH, Koper MTM (2006) J Phys Chem B 110:10021
96. Maillard F, Savinova ER, Stimming U (2007) J Electroanal Chem 599:221